Laminar forced convection in circular microchannels with slip-flow: Analysis of randomly distributed roughness

Laminar forced convection in circular microchannels with slip-flow: analysis of randomly distributed roughness

L. A. Sphaier[a,*], A. Barletta[b], M. Celli[b], P. V. Brandão[b], E. Ghedini[b]

[a] *Laboratory of Thermal Sciences – LATERMO, Department of Mechanical Engineering – PGMEC/TEM, Universidade Federal Fluminense – UFF*
Rua Passo da Pátria 156, bloco D, sala 302, Niterói, RJ, 24210-240, Brazil
[b] *Department of Industrial Engineering, Alma Mater Studiorum Università di Bologna, Viale Risorgimento 2, 40136 Bologna, Italy*

Abstract

This paper investigates the sensitivity of heat transfer and fluid flow to geometric uncertainties caused by roughness in microchannels. The study considers laminar, fully developed slip flow and temperature jump conditions in the momentum and energy equations, controlled by velocity slip (λ) and temperature jump (λ_T) parameters, under traditional H1 and H2 heating conditions. Microchannels with nominally circular geometries are analyzed, incorporating random boundary variations defined by a roughness parameter, $\delta r^*_{\max}$. These variations generate unique geometries for each $\delta r^*_{\max}$, grouped into samples for numerical simulation and statistical analysis. The analysis shows that for every configuration, a normal distribution of Poiseuille and Nusselt numbers values is obtained for each $\delta r^*_{\max}$. An examination of the median and standard deviation of each sample reveals that increasing $\delta r^*_{\max}$ leads to higher Poiseuille numbers and lower Nusselt numbers, indicating greater pressure drop and reduced heat transfer, respectively. The influence of slip length and temperature jump parameters was also assessed, revealing that while higher λ values reduce the friction factor, these cases are more impacted by roughness. Conversely, although an increase in λ_T significantly reduces the Nusselt number due to added thermal resistance, cases with lower λ_T are more sensitive to roughness effects.

Keywords: pressure drop, friction factor, Poiseuille number, heat transfer, Nusselt number, statistical analysis

1. Introduction

Since the experiments conducted by Nikuradse et al. [1], it has generally been understood in the literature that relatively small surface roughness does not affect friction factor calculations in laminar flows. However, later experiments demonstrated that wall surface

*Corresponding author. Phone: +55 21 2629-5582. Fax: +55 21 2629-5419
Email address: lasphaier@id.uff.br (L. A. Sphaier)

roughness does, in fact, impact laminar friction factor calculations in microchannels [2, 3]. According to Mala and Li [3], conventional theory agreed well with experimental results at low flow velocities but lost validity at higher velocities. Kandlikar [4, 5] highlighted the uncertainties in Nikuradse's original experiments, emphasizing the role of surface roughness in mini and microchannels. In practice, surface roughness is unavoidable, and such effects are expected to impact micro-devices more significantly due to high manufacturing uncertainties and the small dimensions involved.

For what concerns the heat transfer characteristics, Wu and Little [6] have found experimentally that, as well as for the friction factor calculations, roughened microchannels have an improved heat transfer coefficient for fully turbulent flows. However, Peng et al. [7] found different correlations for the heat transfer coefficient for laminar flows in microchannels. In their study, the new correlations indicate smaller values of the heat transfer coefficient for microchannel flows. While Weaver et al. [8] have observed experimentally a friction factor augmentation even for relatively small surface roughness, an augmentation in the heat transfer coefficient was observed just for relatively high surface roughness in microchannels with manufacturing roughness levels. A good review on experimental results of fluid flow and heat transfer at micro and meso-scales can be found in the work by Mehendale et al. [9].

It is important to note that the dynamics of microchannel flows does not always align with conventional fluid dynamics. A comprehensive review of fluid flow phenomena specific to microdevices is provided by Gad-el Hak [10]. Different flow regimes can be identified based on the Knudsen number (Kn), which is the ratio between the mean free path of molecules and a characteristic length of the domain in question. For $\mathrm{Kn} \leq 10^{-3}$, the Navier-Stokes equations with no-slip boundary conditions remain valid, while for $10^{-3} \leq \mathrm{Kn} \leq 10^{-1}$, slip boundary conditions must be applied to the Navier-Stokes equations. For instance, considering air at standard temperature and pressure within a microdevice of $1\,\mu$m yields $\mathrm{Kn} \sim O(10^{-2})$, indicating a slip-flow regime [10]. Shu et al. [11] present an extensive review of fluid velocity slip and temperature jump at solid surfaces.

Sun and Faghri [12] investigated the effect of surface roughness on nitrogen flow in a microchannel using Monte Carlo direct simulation. They modeled surface roughness as an array of uniformly placed rectangular modules on both walls of a parallel horizontal channel. According to their findings, surface roughness effects are more pronounced at low Knudsen numbers, resulting in higher friction factors compared to smooth surfaces. Conversely, at higher Knudsen numbers, rarefaction effects reduce the friction factor relative to smooth channels. Their friction factor calculations were based on the nominal hydraulic diameter. Kleinstreuer and Koo [13] examined the effects of surface roughness on liquid flow in microconduits, modeling wall roughness as a porous medium layer. Their results qualitatively agreed with previous findings and experimental data, showing an increase in the friction factor when surface roughness was accounted for. They used the actual hydraulic diameter in their calculations. Similarly, Duan and Muzychka [14] studied the impact of surface roughness on laminar flow in microtubes by modeling roughness as a sinusoidal wave. Using the actual hydraulic diameter, they observed an increase in the friction factor with roughness.

Fewer numerical investigations on the effects of roughness on heat transfer coefficients

in microchannel flows are available in the literature. Classical results on the impact of roughness on forced convection in laminar flow within conventional ducts are provided in Shah and London [15]. Using the actual hydraulic diameter in their calculations, they observed a decrease in the heat transfer coefficient with increasing wall roughness. Sadeghi et al. [16] studied the effects of corrugated roughness on forced convection in gaseous slip flow within microtubes, modeling surface roughness as a sinusoidal wave and using the actual hydraulic diameter in their calculations. For slip flows, Sadeghi et al. [16] found a qualitative agreement with the results reported by Shah and London [15], observing that roughness led to an increase in the friction factor and a decrease in the heat transfer coefficient.

The present work is aimed at investigating the effect of surface roughness on heat transfer and fluid flow characteristics of fully developed flows in nominally circular microchannels. To achieve this, roughness is considered within the channel cross-section rather than along the main flow direction. Surface roughness is represented by introducing random variations in the positions that define a nominal circle. The effects are analyzed for different relative roughness values, varying slip flow parameters (velocity slip and temperature jump), and the heat transfer boundary conditions H1 and H2. The nominal hydraulic diameter is adopted for all calculations. The novelty of this work lies in the use of randomly generated surface roughness within the channel cross-section, enabling a detailed analysis of roughness effects on heat transfer and fluid flow in microchannels that reflects more realistic geometric variations beyond traditional smooth or uniformly rough models.

2. Problem description

The problem herein considered is that of a cylindrical microchannel with a nominally circular cross-section. Small variations in its cross-section geometry are considered, hence departing from the atual circular geometry, which would be obtained for perfectly smooth channels. These variations from the actual nominal shape represent the roughness of the channel, and are due to the practical manufacturing issues whatever are the adopted fabrication techniques. Hence, although the nominal cross-section is a circle with radius R, the perimeter of the duct cross-section with be denoted $\mathcal{P}$ having and encompassing area of $\mathcal{S}$, as illustrated in figure 1. As seen in this figure, the nominal geometry is plotted in gray, while the actual geometry is constructed by taking points evenly distributed on the nominal geometry boundary and allowing for a random variation in both the tangential and normal directions. This is accomplished by prescribing these points on locations given by the the general position vector, expressed in polar coordinates as:

$$\mathbf{r} = (R + \delta R)(\cos(\varphi + \delta\varphi), \sin(\varphi + \delta\varphi)), \tag{1}$$

where φ varies within $0 \leq \varphi < 2\,\pi$ with a step given by $2\,\pi/n_{pts}$. The random tangential variation is thus specified by $\delta\varphi$, which is allowed to randomly vary within $\pm\,\pi/n_{pts}$, so as to prevent two neighboring point from overlapping. The random normal variation is achieved by moving the point in that direction by an amount given by δr_n, where this amount is randomly varied for every point such that $-\delta R \leq \delta r_n \leq \delta R$. Hence, the parameters that control the randomly generated roughness are n_{pts} and $\delta r^*_{\max} = \delta R/R$.

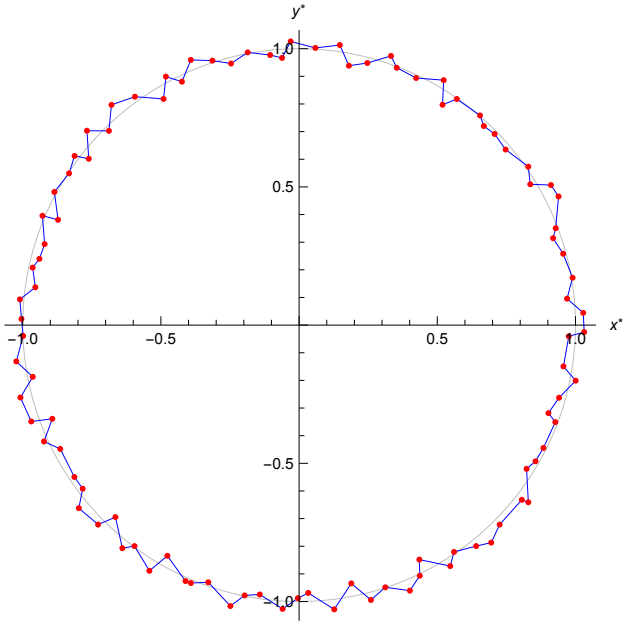

Figure 1: Problem domain: nominal and real randomly-generated geometry.

Once the points associated to random variations on the duct geometry are generated, the resulting geometry is obtained by connecting the resulting points by straight lines (i.e. linear interpolation) effectively generating an irregular polygon for representing the channel cross-section boundary. Although one could argue that perfectly smooth channels could be obtained involves setting $\delta\varphi = 0$ and $\delta R = 0$, this does not lead to exactly circular channels, but rather to a regular polygon with n_{pts} vertices. This in fact is the case, but since the solution methodology herein involves discretizing the domain using triangular finite elements, the boundary will ultimately be approximated by a polygon, and sufficiently large number of boundary points will be selected to ensuring when $\delta\varphi = \delta R = 0$ the results match, to minimum prescribe tolerance, those of a perfect circle.

The actual hydraulic diameter of the irregular geometry is defined as:

$$D_h = \frac{4\,\mathcal{S}}{\mathcal{P}}. \tag{2}$$

As this study deals with ducts with random deviations in the cross section geometry, D_h will be considered the actual hydraulic diameter for a particular case. In addition, the nominal hydraulic diameter associated with a given case will be referred to as $\hat{D}_h$, which for an circular duct is simply given by $2\,R$.

2.1. Governing equations

Considering laminar, steady, incompressible and fully-developed flow, the only nonzero component of the velocity field is in the axial direction (denoted as z) and is denoted with u. Local mass balance (i.e. the continuity equation) naturally requires that u be independent of z, such that $u = u(x, y)$, where x and y are the Cartesian coordinates in the

cross-sectional plane. Finally, the local difference between the pressure and the hydrostatic pressure (denoted as $p(z)$) depends soley on z. Hence, the local momentum balance equation is expressed as

$$\nabla^2 u = \frac{1}{\mu}\frac{\mathrm{d}p}{\mathrm{d}z}, \quad (x, y) \in \mathcal{S}, \tag{3}$$

where $\mathrm{d}p/\mathrm{d}z$ is a constant pressure gradient and μ denotes the dynamic viscosity. This equation is subjected to the boundary condition

$$u + \lambda\, \mathbf{n} \cdot \boldsymbol{\nabla} u = 0, \quad (x, y) \in \mathcal{P}, \tag{4}$$

where $\lambda > 0$ is the slip length [17] and the vector $\mathbf{n}$ is the unit outward normal to $\mathcal{P}$.

The thermal boundary conditions contemplated in this work are either H1 or H2 according to the classification defined by Shah and London [18]. Figure 2 provides a simple schematic illustration of the two heat transfer boundary conditions. One should recall that condition

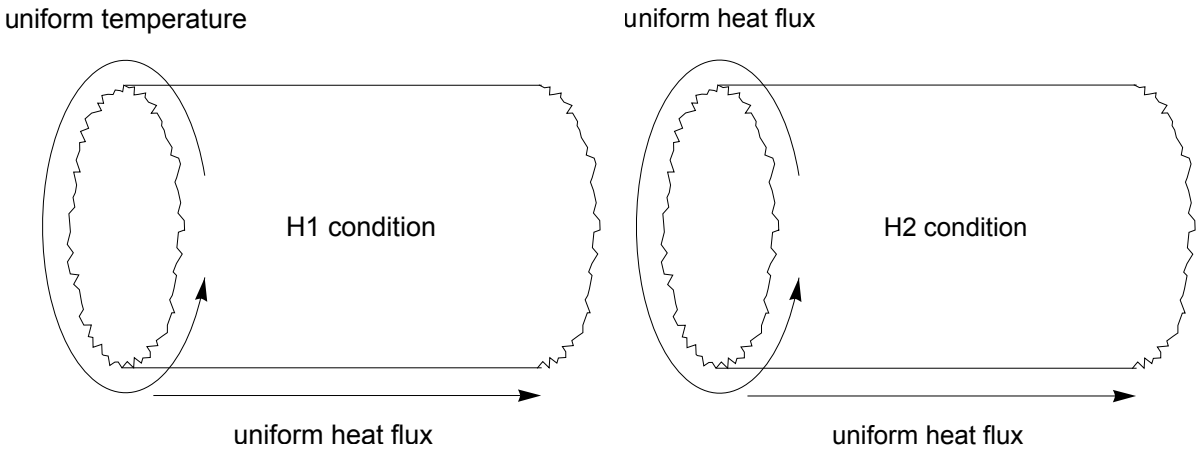

Figure 2: Schematic representation of the two heat transfer boundary conditions.

H1 means a peripherally uniform wall temperature and a longitudinally uniform wall heat flux, while H2 means a peripherally and longitudinally uniform wall heat flux. It is also well-known that conditions H1 and H2 coincide when $\mathcal{P}$ is exactly a circle [18], which would be the case for a perfectly smooth circular channel. Furthermore, the boundary conditions H1 and H2 imply that the derivative $\partial T/\partial z$ is a constant [18, 19], hereafter denoted as a. Thus, the local energy balance equation is given by [18, 19],

$$\alpha\, \nabla^2 T - a\, u = 0, \tag{5}$$

where α is the thermal diffusivity of the fluid.

The boundary condition usually with slip flow can be written in a general form as:

$$(T - T_w) \;+\; \lambda_T\, \mathbf{n} \cdot \boldsymbol{\nabla} T \;=\; 0, \quad (x, y) \in \mathcal{P}, \tag{6}$$

where $T_w(x, y)$ is the solid wall temperature, and $T(x, y)$ at positions on $\mathcal{P}$ represents the fluid temperature at the wall, which can be different from T_w due to the temperature jump condition. The inward heat flux at the wall is written as:

$$q_w \;=\; k\,\mathbf{n}\cdot\boldsymbol{\nabla}T, \quad (x,y)\in\mathcal{P}. \tag{7}$$

As previously recalled, for the H1 conditions T_w is independent of (x, y), while q_w can vary along the periphery, while for the H2 condition perimeter-averaged heat flux $\bar{q}_w$ is constant for a given z, while the wall temperature T_w varies along the periphery. Regardless of the type of boundary condition, the perimeter-averaged values for these parameters are defined as:

$$\bar{T}_w \;=\; \frac{1}{\mathcal{P}}\int_{\mathcal{P}} T_w\,\mathrm{d}\mathcal{P}, \quad \text{and} \quad \bar{q}_w \;=\; \frac{1}{\mathcal{P}}\int_{\mathcal{P}} q_w\,\mathrm{d}\mathcal{P}. \tag{8}$$

With either conditions H1 or H2, it is easily verified that the mean wall heat flux $\bar{q}_w$ is a constant and the constant a not only coincides with $\partial T/\partial z$, but also with $\mathrm{d}\bar{T}_w/\mathrm{d}z$ and $\mathrm{d}T_b/\mathrm{d}z$, where T_b is the bulk temperature, i.e.

$$\frac{\partial T}{\partial z} = \frac{\mathrm{d}\bar{T}_w}{\mathrm{d}z} = \frac{\mathrm{d}T_b}{\mathrm{d}z} = a, \quad \text{with} \quad T_b = \frac{1}{\mathcal{S}\,u_m}\int_{\mathcal{S}} T\,u\,\mathrm{d}\mathcal{S}, \tag{9}$$

where the bulk or mean-stream velocity is defined as:

$$u_m = \frac{1}{\mathcal{S}}\int_{\mathcal{S}} u\,\mathrm{d}\mathcal{S}. \tag{10}$$

The integration of equation (5) within the cross section yields a global energy balance, which results in the following relation for the axial temperature gradient:

$$a \;=\; \frac{\mathcal{P}}{\mathcal{S}}\,\frac{\bar{q}_w}{\rho\,c_p\,u_m}, \tag{11}$$

in which ρ is the fluid density and c_p is its constant pressure specific heat.

Having defined the previous parameters, the Nusselt number is given by [18]:

$$\mathrm{Nu} \;=\; \frac{h\,\hat{D}_h}{k} \;=\; \frac{\hat{D}_h}{k}\,\frac{\bar{q}_w}{\bar{T}_w - T_b}, \tag{12}$$

where h is the cross-section-averaged convective heat transfer coefficient. At this point, one should highlight that, a priori, the only known information about the duct geometry is that, nominally, its cross section is circular with a nominal diameter $\hat{D}_h$. For this reason $\hat{D}_h$ is used in the definition of the Nusselt number. If the channel were perfectly smooth $\bar{q}_w$, $\bar{T}_w$ and T_b would match that for a perfect circular geometry. However, the roughness will have a tendency to require a larger temperature difference $\bar{T}_w - T_b$ for the same average heat flux

$\bar{q}_w$, due to additional thermal resistance, such that Nusselt number values generally smaller than those obtained for smooth channels can be expected.

Finally, observing the previous expressions, one notices that the temperature jump condition (equation (6)) is used as a boundary condition only for the H1 case. For the heat flux condition H2, (6) is not required for solving the PDE system; nevertheless, it is employed for calculating T_w.

2.2. Dimensionless formulation

The dimensionless quantities and operators employed in thus study are defined as:

$$(x^*, y^*) = \frac{(x, y)}{R}, \quad \nabla^* = R\,\nabla, \quad u^* = \frac{u}{u_0}, \quad T^* = k\,\frac{T - \bar{T}_w}{\bar{q}_w\,R}, \tag{13}$$

where k is the fluid thermal conductivity and u_0 is a constant reference velocity defined as

$$u_0 = -\frac{2\,R^2}{\mu}\,\frac{\mathrm{d}p}{\mathrm{d}z}. \tag{14}$$

Employing the definition of the Fanning friction factor [18], and its relation to the Poiseuille number, yields

$$f\,\mathrm{Re} \;=\; \mathrm{Po} \;=\; -\frac{\hat{D}_h^2}{2\,\mu\,u_m}\frac{\mathrm{d}p}{\mathrm{d}z}, \tag{15}$$

where $\mathrm{Re} = u_m\,\hat{D}_h/\nu$ is the Reynolds number based on the nominal hydraulic diameter $\hat{D}_h$. Employing definitions (10) and (14) leads to

$$\frac{u_0}{u_m} = \mathrm{Po}. \tag{16}$$

The dimensionless hydraulic diameter D_h^* is defined as:

$$D_h^* \;=\; \frac{D_h}{2\,R} \;=\; \frac{2\,\mathcal{S}^*}{\mathcal{P}^*}, \tag{17}$$

where the symbols $\mathcal{P}^*$ and $\mathcal{S}^*$ denote the dimensionless geometric objects obtained from $\mathcal{P}$ and $\mathcal{S}$ with the coordinates scaled by the reference length R:

$$\mathcal{S}^* \;=\; \frac{\mathcal{S}}{R^2}, \qquad \mathcal{P}^* \;=\; \frac{\mathcal{P}}{R}. \tag{18}$$

At this point one should point out that by calculating $f\,\mathrm{Re}$ from equation (15), as similarly pointed out in the definiton of the Nusselt number, one obtains the value of the Poiseuille number for a nominally circular channel, but with the addition of the roughness effect. As a result, higher Po values are expected as smaller flow rates per channel area (and hence smaller mean velocities u_m) will be obtained for a prescribed pressure gradient $\mathrm{d}p/\mathrm{d}z$, when compared to a perfectly smooth channel.

On account of (13), one can rewrite (3) as

$$\nabla^{*2} u^* + \frac{1}{2} = 0, \tag{19}$$

to be solved by employing the boundary condition

$$u^* + 2\,\lambda^*\,\mathbf{n}\cdot\nabla^* u^* = 0, \quad (x^*, y^*) \in \mathcal{P}^*, \tag{20}$$

where the dimensionless slip parameter λ^* is defined as

$$\lambda^* = \frac{\lambda}{2\,R}. \tag{21}$$

After solving (19) and (20), one can evaluate Po by employing (14)-(16) which yields

$$\mathrm{Po} = \frac{\mathcal{S}^*}{\displaystyle\int_{\mathcal{S}^*} u^*\,\mathrm{d}\mathcal{S}^*}. \tag{22}$$

Using the dimensionless parameters (13), the local energy balance (5) is rewritten as

$$\nabla^{*2} T^* - \frac{2\,\mathrm{Po}}{D_h^*}\,u^* = 0, \tag{23}$$

where the associated boundary conditions are alternatively given as

$$T^* + 2\,\lambda_T^*\,\mathbf{n}\cdot\nabla^* T^* = 0, \quad (x^*, y^*) \in \mathcal{P}^*, \quad \text{for the H1 condition,} \tag{24a}$$

$$\mathbf{n}\cdot\nabla^* T^* = 1, \quad (x^*, y^*) \in \mathcal{P}^*, \quad \text{for the H2 condition,} \tag{24b}$$

where λ_T^* is the dimensionless version of λ_T:

$$\lambda_T^* = \frac{\lambda_T}{2\,R}. \tag{25}$$

In addition, while $T_w^* = 0$ for the H1 condition, for the H2 condition, the wall temperature can be obtained from:

$$T_w^* = T^* + 2\,\lambda_T^*. \tag{26}$$

Finally, it is important to recall that in the special case of a perfect circular geometry, the two boundary conditions H1 and H2 coincide [18]. This is a consequence of the special geometrical symmetry of the circle, which is broken by irregularities on the duct surface. These irregularities arise when random variations are introduced in the channel boundary and can also occur even when $\delta\varphi = \delta R = 0$, due to the boundary being approximated by a finite number of points; however, these differences diminish as the number of boundary points increases, progressively approximating the geometry of a perfect circle.

2.3. Nusselt number evaluation

Using the previous dimensional relations, the Nusselt number can be written as

$$\mathrm{Nu} \;=\; \frac{2}{\bar{T}_w^* - T_b^*}. \tag{27}$$

Hence, after determining of u^*, T^* and T_w^*, one can finally evaluate the Nusselt number from (27), where:

$$T_b^* \;=\; \frac{\mathrm{Po}}{\mathcal{S}^*} \int_{\mathcal{S}^*} T^*\, u^*\, \mathrm{d}\mathcal{S}^*, \tag{28}$$

and $\bar{T}_w^*$ is calculated from

$$\bar{T}_w^* \;=\; \frac{1}{\mathcal{P}^*} \int_{\mathcal{P}^*} T_w^*\, \mathrm{d}\mathcal{S}^*, \tag{29}$$

where, naturally, $\bar{T}_w^* = 0$ for the H1 condition.

2.4. Perfectly smooth micro-channels

Recalling the well-known results relative to an exactly circular cross-section may be useful for the forthcoming discussion of the results. In the absence of any roughness, the dimensionless velocity resulting from the simple analytical solution of the governing equations in a one-dimensional circular domain yields a generalized Hagen-Poiseuille profile:

$$u^* = \frac{1}{8}\big(1 - r^{*2} + 2\lambda^*\big), \tag{30}$$

$$T^* = \frac{\big(1 - r^{*2}\big)\,\big(r^{*2} - 16\lambda - 3\big)}{32\,\lambda^* + 4} \;-\; 2\,\lambda_T^*, \tag{31}$$

with $r^* = \sqrt{x^{*2} + y^{*2}}$. Moreover, $\mathcal{S}^* = \pi$, $\mathcal{P}^* = 2\pi$ and the Poiseuille and Nusselt number are given by:

$$\hat{\mathrm{Po}} = \frac{16}{1 + 4\lambda^*}, \tag{32}$$

$$\hat{\mathrm{Nu}} \;=\; \frac{48(8\lambda^* + 1)^2}{48(8\lambda^* + 1)^2\,\lambda_T^* + 128\lambda^*(3\lambda^* + 1) + 11}, \tag{33}$$

remembering that for this case, both the H1 and H2 condition give the same results. Naturally, for $\lambda^* = \lambda_T^* = 0$, the classical results with $\hat{\mathrm{Po}} = 16$ and $\hat{\mathrm{Nu}} = 48/11$ are obtained. Here the notation $\hat{\mathrm{Po}}$ and $\hat{\mathrm{Nu}}$ adopted to emphasize that these values correspond to the nominal values, obtained for a perfectly smooth channel.

3. Numerical methodology

The computational implementation involves solving the PDE system defined by equations (19) and (23), subject to the boundary conditions (20) and (24), to determine the Poiseuille and Nusselt numbers. The solution process utilizes the Finite Element Method (FEM) to handle the irregular geometries introduced by the random boundary variations. The channel geometries are discretized into triangular element meshes, with mesh sizes controlled by a user-defined parameter related to the maximum cell measure. The complete solution process for a given random geometry channel can be summarized by the following steps, using as input parameters values for n_{pts}, $\delta r^*_{\max}$, λ^*, and λ^*_T:

1. **Geometry Generation:** The random channel geometry is generated based on equation (1), using a uniform random distribution for the variations, constrained by the parameters n_{pts} and $\delta r^*_{\max}$.
2. **Mesh Discretization:** The channel cross-section is discretized into a FEM mesh, enabling numerical calculations over the irregular domain.
3. **Geometric Properties:** The dimensionless area $\mathcal{S}^*$ and perimeter $\mathcal{P}^*$ are calculated numerically, followed by the hydraulic diameter D^*_h using equation (17).
4. **Velocity Field Solution:** The dimensionless velocity field u^* is solved numerically using equations (19) and (20).
5. **Friction Factor Calculation:** The Poiseuille number Po is determined using equation (22).
6. **Temperature Field Solution for H1:** The temperature field T^* is calculated for the H1 condition using equations (23) and (24a), followed by the bulk temperature T^*_b and Nusselt number $\mathrm{Nu}_{\mathsf{H1}}$ from equations (28) and (27).
7. **Temperature Field Solution for H2:** The temperature field T^* is calculated for the H2 condition using equations (23) and (24b), followed by T^*_b, wall temperature $\bar{T}^*_w$, and $\mathrm{Nu}_{\mathsf{H2}}$ using equations (28), (29), and (27).

This procedure is repeated for each random geometry, ensuring a unique solution for each simulation due to the variability in the boundary. Special cases, such as $\delta r^*_{\max} = 0$ and $\delta\varphi = 0$, produce regular polygonal geometries and are used for verification purposes. For each combination of n_{pts}, $\delta r^*_{\max}$, λ^*, and λ^*_T, multiple geometries are simulated, with the computations performed in parallel to enhance efficiency.

The implementation makes use of various *Mathematica* functions to streamline the computational process. The random geometries are generated using **RandomReal**, while FEM meshes are created with **DiscretizeRegion** and **ToElementMesh**. The governing equations are solved using **NDSolve** and the finite element package **NDSolve‘FEM‘**, with mesh size controlled by the **MaximumCellMeasure** parameter. Numerical integrations required for calculating $\mathcal{P}^*$, $\mathcal{S}^*$, Po, and Nu are performed using **NIntegrate**. The parallel processing of multiple geometries is accomplished with **ParallelDo**, ensuring computational efficiency for large sample sizes.

4. Results and discussion

4.1. Verification of numerical solution

The first set of results presented is aimed at verifying the employed methodology and numerical implementation. Initially, a convergence analysis is performed, with results compared to the analytical solution for perfectly smooth circular channels, as presented in section 2.4. The convergence analysis involves varying the spatial discretization size through the parameter **MaxCellMeasure** (MCM), which controls the size of the finite element cells used in the discretization. Additionally, since the microchannel boundary is effectively approximated by a polygon, the number of boundary points, n_{pts}, is also varied. However, for this verification step, the parameters $\delta r^*_{\max}$ and $\delta\varphi$ are set to zero to allow proper comparison with the data for a perfectly smooth channel. As the number of boundary points increases, one can expect the polygonal duct results to gradually converge to those of the circular duct. Tables 1 and 2 present results for different values of MCM and n_{pts}. The results include the geometric parameters $\mathcal{P}^*$ and $\mathcal{S}^*$, as well as the Poiseuille and Nusselt numbers calculated for different values of λ^* and λ^*_T. As can be seen, the discretization parameter MCM has a more pronounced effect on cases with a smaller number of boundary points, n_{pts}. This occurs because using more boundary points also impacts the size of the triangular finite element cells, forcing them to become smaller as n_{pts} increases. While this is evident for the geometric parameters $\mathcal{P}^*$ and $\mathcal{S}^*$ and the Poiseuille number, where 200 boundary points yield the exact same results across all MCM values, for the Nusselt numbers, even for 1600 boundary points, MCM values of 10^{-3} are required for a obtaining a converged solution. This naturally indicates that calculating Nusselt numbers demands finer meshes.

Observing the values of the Poiseuille number, Nusselt numbers and geometric parameters as n_{pts} increases, one finds that 1600 boundary points yield results matching the exact values up to the full six digits for $\mathrm{Nu}_{\mathsf{H1}}$ and $\mathrm{Nu}_{\mathsf{H2}}$ regardless of the values of λ^* or λ^*_T. The same precision is seen for the Po values when $\lambda^* = 0$. At the same time, for the geometric parameters $\mathcal{P}^*$ and $\mathcal{S}^*$, and for the Poiseuille number for $\lambda^* = 0.01$ and 0.1, the results with $n_{pts} = 1600$ match the exact values up to the fifth significant digit. Moreover, a precision of 4 significant digits is generally obtained with 400 boundary points. While these higher levels of precision are found for a large number of boundary points, one notices that employing $n_{pts} = 100$ also yield results consistent with those of a circular channel, with an error below 0.1%. Since CPU time increases significantly with both n_{pts} and MCM, values of $n_{pts} = 100$ and MCM $= 10^{-3}$ will be used for the results presented in the remainder of this text.

After the previous verification results, an illustration of velocity and temperature profiles is provided for clarity. Figure 3 displays the calculated flow and temperature fields for the two heat transfer boundary conditions in a randomly generated geometry with 100 boundary points and $\delta r^*_{\max} = 0.05$. The results are presented for both a no-slip condition ($\lambda^* = \lambda^*_T = 0$) and a slip condition ($\lambda^* = \lambda^*_T = 0.1$). As can be seen, the velocity plot for the no-slip condition shows a region near the wall with low velocities, as expected. Under the slip condition with $\lambda^* = 0.1$, such low-velocity regions become practically nonexistent, and the core fluid velocity exhibits higher values, resulting in increased flow rates for these conditions. When examining the temperature plots, the cases with $\lambda^* = \lambda^*_T = 0$ may initially

Table 1: Verification: Poiseuille number and geometrical parameters values for different number of points and MaxCellSize (MCM) parameters for different number of points.

		Po				
n_{pts}	MCM	$\lambda^* = 0$	$\lambda^* = 0.01$	$\lambda^* = 0.1$	$\mathcal{P}^*$	$\mathcal{S}^*$
25	0.1	16.2020	14.9786	8.97306	6.26666	3.10862
25	0.01	16.1814	14.9746	8.97301	6.26666	3.10862
25	0.001	16.1792	14.9740	8.97300	6.26666	3.10862
25	0.0001	16.1790	14.9740	8.97300	6.26666	3.10862
50	0.1	16.0463	14.8539	8.90975	6.27905	3.13333
50	0.01	16.0451	14.8538	8.90975	6.27905	3.13333
50	0.001	16.0435	14.8536	8.90974	6.27905	3.13333
50	0.0001	16.0434	14.8536	8.90974	6.27905	3.13333
100	0.1	16.0111	14.8244	8.89409	6.28215	3.13953
100	0.01	16.0111	14.8244	8.89409	6.28215	3.13953
100	0.001	16.0107	14.8244	8.89409	6.28215	3.13953
100	0.0001	16.0107	14.8244	8.89409	6.28215	3.13953
200	0.1	16.0027	14.8172	8.89019	6.28293	3.14108
200	0.01	16.0027	14.8172	8.89019	6.28293	3.14108
200	0.001	16.0027	14.8172	8.89019	6.28293	3.14108
200	0.0001	16.0027	14.8172	8.89019	6.28293	3.14108
400	0.1	16.0007	14.8154	8.88921	6.28312	3.14146
400	0.01	16.0007	14.8154	8.88921	6.28312	3.14146
400	0.001	16.0007	14.8154	8.88921	6.28312	3.14146
400	0.0001	16.0007	14.8154	8.88921	6.28312	3.14146
800	0.1	16.0002	14.8150	8.88897	6.28317	3.14156
800	0.01	16.0002	14.8150	8.88897	6.28317	3.14156
800	0.001	16.0002	14.8150	8.88897	6.28317	3.14156
800	0.0001	16.0002	14.8150	8.88897	6.28317	3.14156
1600	0.1	16.0000	14.8149	8.88891	6.28318	3.14158
1600	0.01	16.0000	14.8149	8.88891	6.28318	3.14158
1600	0.001	16.0000	14.8149	8.88891	6.28318	3.14158
1600	0.0001	16.0000	14.8149	8.88891	6.28318	3.14158
exact	—	16.0000	14.8148	8.88889	6.28319	3.14159

appear similar; however, the characteristics of the H1 and H2 boundary conditions become evident in the boundary temperature distributions. For the H1 condition, the boundary temperature is uniform, whereas for the H2 condition, the heat flux is uniform, leading to temperature fluctuations along the boundary. These plots suggest that, for this geometry, the H2 boundary condition results in a lower bulk temperature T_b^*, as a larger amount of fluid in the channel center is at lower temperatures. This contributes to an increased temperature difference $T_w^* - T_b^*$, which should lead to lower Nusselt number values. For the presented slip condition, which includes the temperature jump boundary condition with $\lambda_T^* = 0.1$, the

Table 2: Verification: Nusselt number values for different number of points and MaxCellSize (MCM) parameters for different number of points.

		$\lambda^* = \lambda_T^* = 0$		$\lambda^* = \lambda_T^* = 0.01$		$\lambda^* = \lambda_T^* = 0.1$	
n_{pts}	MCM	$\mathrm{Nu}_{\mathsf{H1}}$	$\mathrm{Nu}_{\mathsf{H2}}$	$\mathrm{Nu}_{\mathsf{H1}}$	$\mathrm{Nu}_{\mathsf{H2}}$	$\mathrm{Nu}_{\mathsf{H1}}$	$\mathrm{Nu}_{\mathsf{H2}}$
25	0.1	4.38137	4.37449	4.36195	4.36195	3.60813	3.60813
25	0.01	4.37546	4.37344	4.35904	4.35904	3.60766	3.60766
25	0.001	4.37536	4.37371	4.35899	4.35899	3.60766	3.60766
25	0.0001	4.37536	4.37373	4.35899	4.35899	3.60766	3.60766
50	0.1	4.36708	4.36635	4.35059	4.35059	3.60248	3.60248
50	0.01	4.36666	4.36617	4.35032	4.35032	3.60242	3.60242
50	0.001	4.36652	4.36631	4.35027	4.35027	3.60241	3.60241
50	0.0001	4.36652	4.36633	4.35027	4.35027	3.60241	3.60241
100	0.1	4.36453	4.36444	4.34826	4.34826	3.60113	3.60113
100	0.01	4.36439	4.36431	4.34815	4.34815	3.60111	3.60111
100	0.001	4.36436	4.36432	4.34813	4.34813	3.60110	3.60110
100	0.0001	4.36436	4.36433	4.34813	4.34813	3.60110	3.60110
200	0.1	4.36390	4.36389	4.34767	4.34767	3.60079	3.60079
200	0.01	4.36383	4.36382	4.34760	4.34760	3.60078	3.60078
200	0.001	4.36382	4.36381	4.34759	4.34759	3.60078	3.60078
200	0.0001	4.36382	4.36381	4.34759	4.34759	3.60078	3.60078
400	0.1	4.36376	4.36376	4.34753	4.34753	3.60071	3.60071
400	0.01	4.36369	4.36369	4.34747	4.34747	3.60070	3.60070
400	0.001	4.36368	4.36368	4.34746	4.34746	3.60069	3.60069
400	0.0001	4.36368	4.36368	4.34746	4.34746	3.60069	3.60069
800	0.1	4.36371	4.36371	4.34748	4.34748	3.60069	3.60069
800	0.01	4.36366	4.36366	4.34743	4.34743	3.60068	3.60068
800	0.001	4.36365	4.36365	4.34743	4.34743	3.60067	3.60067
800	0.0001	4.36365	4.36365	4.34743	4.34743	3.60067	3.60067
1600	0.1	4.36369	4.36369	4.34746	4.34746	3.60068	3.60068
1600	0.01	4.36365	4.36365	4.34743	4.34743	3.60067	3.60067
1600	0.001	4.36364	4.36364	4.34742	4.34742	3.60067	3.60067
1600	0.0001	4.36364	4.36364	4.34742	4.34742	3.60067	3.60067
exact	—	4.36364		4.34742		3.60067	

temperature profiles for the H1 and H2 conditions are nearly indistinguishable. This is due to the additional thermal resistance introduced by the λ_T^* parameter, which prevents the enforcement of a uniform boundary temperature for the H1 condition and reduces boundary temperatures for the H2 condition. Examining the core temperatures for this case, even lower T_b^* values are expected. If the overall reduction in T_w^* is not significant, this should lead to lower Nusselt numbers for cases with $\lambda^* = \lambda_T^* = 0.1$. Nevertheless, due to the similarities in the temperature profiles for the H1 and H2 conditions, the resulting Nusselt numbers for these cases are expected to be very similar.

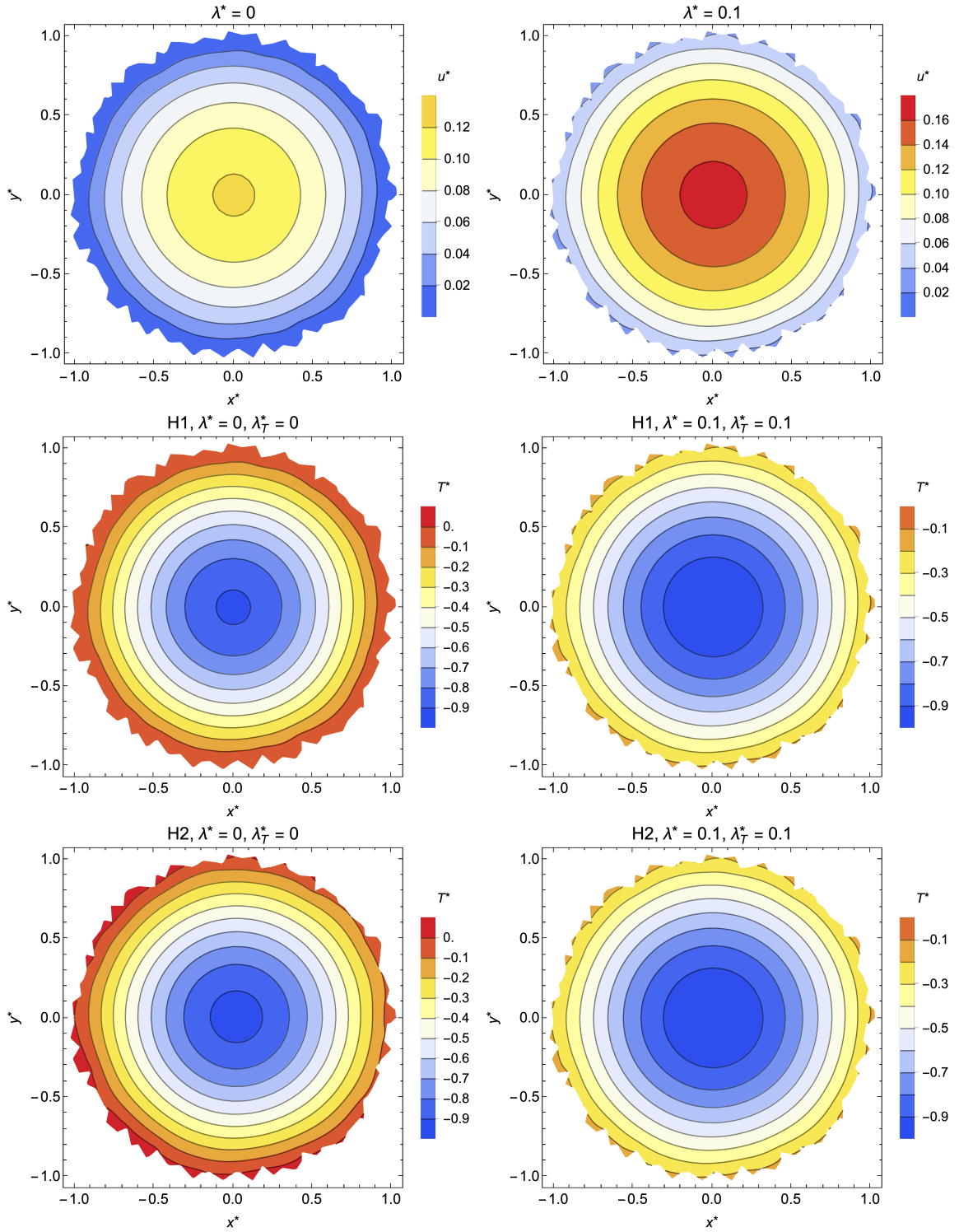

Figure 3: Velocity and temperature contours for a geometry with 100 boundary points and $\delta r^*_{\max} = 0.05$, shown for different values of λ^* and λ^*_T.

4.2. Sample size analysis

Since the channels in this study are generated by randomly varying the position of boundary points within prescribed maximum limits, controlled by $\delta r^*_{\max}$ and n_{pts}, a unique channel geometry is obtained for each simulation. Consequently, rather than analyzing results for individual channels, samples consisting of multiple distinct, randomly generated geometries are used. Although each sample is unique, it is expected that samples generated with the same values of $\delta r^*_{\max}$ and n_{pts} should yield similar median and mean values, provided that sample sizes are sufficiently large. Accordingly, the following results focus on determining an appropriate sample size. Figure 4 shows the calculated mean values of $\mathcal{P}^*$, $\mathcal{S}^*$, Po, $\mathrm{Nu}_{\mathsf{H1}}$, and $\mathrm{Nu}_{\mathsf{H2}}$ for samples of varying sizes. The case with 100 boundary points, $\delta r^*_{\max} = 0.1$, and $\lambda^* = \lambda^*_T = 0$ is selected for illustration purposes. The figures include multiple points for each sample size because, as each sample is randomly generated, variations occur between different samples of the same size; therefore, 100 samples were generated for each sample size. As can be seen, smaller sample sizes exhibit notable differences in mean values across samples of the same size. However, as the sample size increases, the calculated mean values clearly converge to a stable value. The data indicates that the maximum relative variation among calculated mean values occurs for the perimeter $\mathcal{P}^*$. Nevertheless, for sample sizes equal to or greater than 10^5, the maximum observed variation is below 1%, which is considered adequate for this analysis. Although the case with 100 boundary points, $\delta r^*_{\max} = 0.1$, and $\lambda^* = \lambda^*_T = 0$ was used for this sample size analysis, similar behavior is observed across other cases, though not shown here due to space limitations. Also, although the mean values are presented, the same behavior occurs for the median values, as these are practically the same. Following this verification stage, samples of 10^5 geometries will be used for further analysis.

Following the sample size analysis, the distribution of the calculated values for the parameters Po, $\mathrm{Nu}_{\mathsf{H1}}$, and $\mathrm{Nu}_{\mathsf{H2}}$ is examined through histogram plots. These plots are shown for the case with no slip ($\lambda^* = \lambda^*_T = 0$, Figure 5) and for a large value of the slip parameters ($\lambda^* = \lambda^*_T = 0.1$, Figure 6), with $n_{pts} = 100$, and for $\delta r^*_{\max}$ values of 0.01 and 0.10. The results are presented as probability density values, with each histogram overlaid by a normal distribution curve with the same mean and standard deviation as the corresponding sample. As can be seen, the obtained distributions follow a normal distribution and are therefore symmetrical, so the median and mean values are nearly identical (with a maximum observed difference of 0.4), particularly given the large sample size (each with 10^5 cases). Additionally, it is evident that increasing $\delta r^*_{\max}$ from 0.01 to 0.1 results in a notable increase in Po values and a significant decrease in Nu values, with $\mathrm{Nu}_{\mathsf{H2}}$ exhibiting a larger reduction. This tenfold increase in $\delta r^*_{\max}$ also raises the standard deviation (SD) by a factor clearly greater than 10, indicating a strong dependence on the roughness parameter, which will be explored in further detail in the next subsection. Although similar distributions for the geometric quantities $\mathcal{P}^*$ and $\mathcal{S}^*$ are not shown due to space limitations, similar observations regarding the statistical characteristics of the calculated distributions also apply. Likewise, the same holds for cases with other values of $\delta r^*_{\max}$, as well as for other values of λ^* and λ^*_T.

For the sake of complementing the previous results, an analysis is performed on the variation of $\mathcal{P}^*$ and $\mathcal{S}^*$ relative to their nominal values ($2\,\pi$ and π) as the value of $\delta r^*_{\max}$

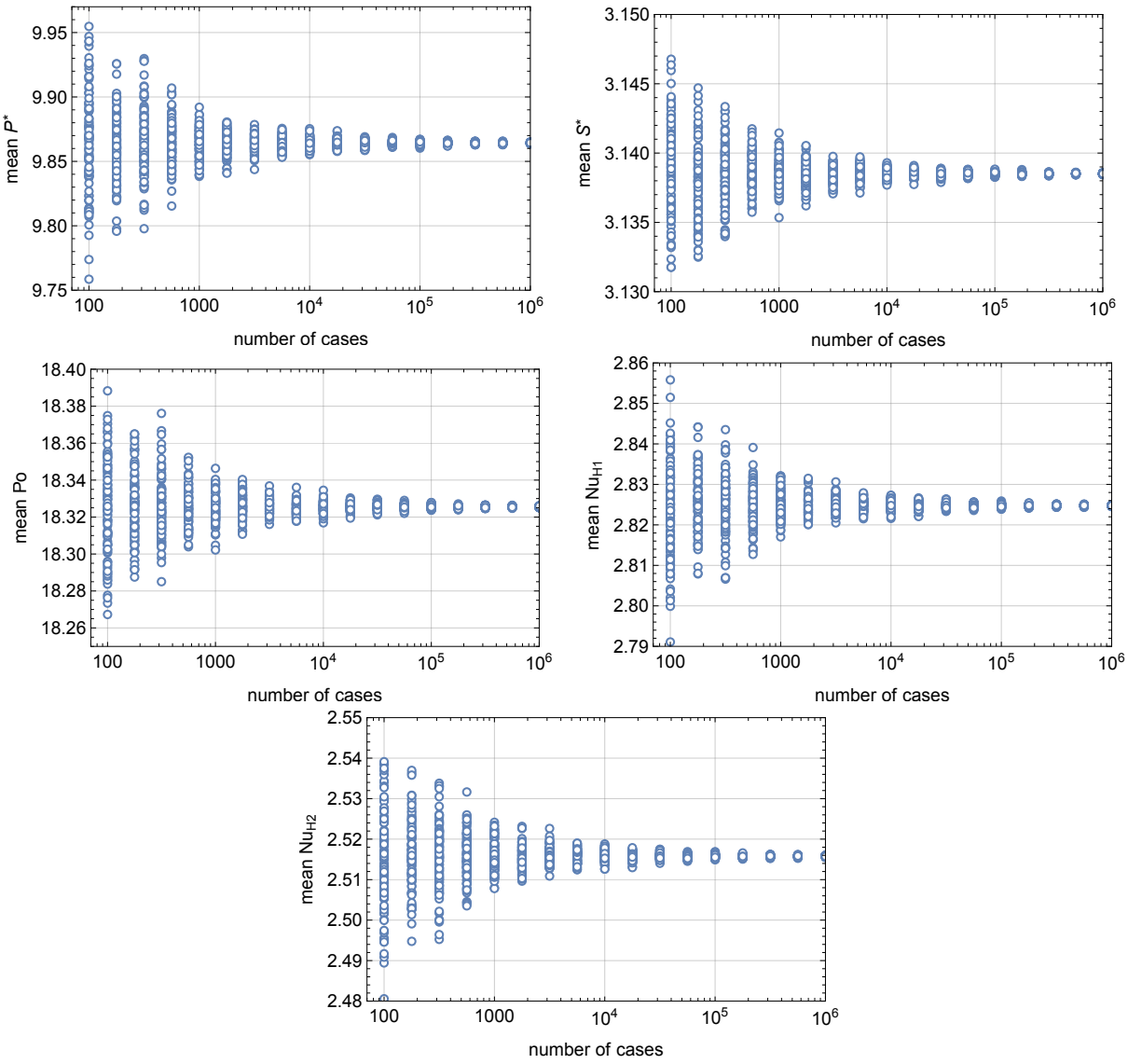

Figure 4: Mean value of $\mathcal{P}^*$, $\mathcal{S}^*$, Po, $\mathrm{Nu}_{\mathrm{H1}}$, and $\mathrm{Nu}_{\mathrm{H2}}$ calculated for random samples of different sizes.

increases. The results are calculated for $n_{pts} = 25$, 50, 100, and 200, and for samples with 10^3, 10^4, and 10^5 cases, as presented in figure 7. The presented results show the mean of each sample, accompanied by error bands plotted as the mean value plus or minus the sample's standard deviation. As seen from the results, the perimeter values $\mathcal{P}^*$ increase with $\delta r^*_{\max}$, while the area $\mathcal{S}^*$ remains relatively unchanged. This is intuitive, as an inward-displaced boundary point reduces the area, while an outward displacement has the opposite effect, resulting in an area that remains nearly constant on average. On the other hand, a randomly displaced boundary point consistently increases the perimeter, regardless of the displacement direction. Indeed, the mean values of $\mathcal{S}^*$ stabilize as sample sizes increase,

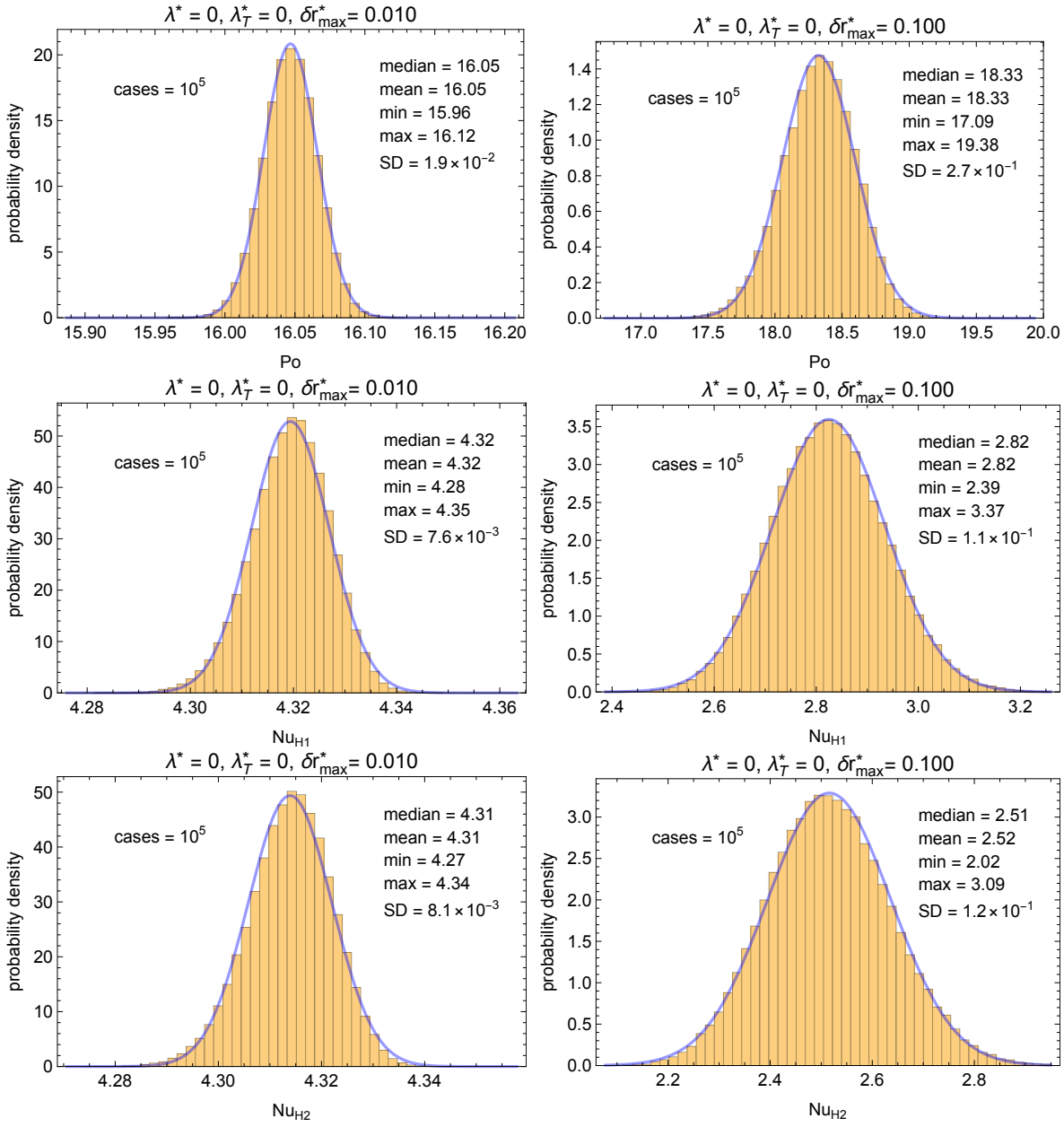

Figure 5: Histogram plots for Poiseuille and Nusselt numbers for $\lambda^* = \lambda_T^* = 0$ calculated for 10^5 random geometries with $n_{pts} = 100$ and $\delta r^*_{\max} = 0.1$.

indicating that the oscillations observed for 10^3 cases, and to a lesser extent for 10^4, are due to insufficient sample sizes. Nevertheless, these fluctuations are less than 1% of $\mathcal{S}^*$. Similar fluctuations occur in smaller samples for $\mathcal{P}^*$, though these are less visible due to the larger scale required to capture the perimeter's significant variation with $\delta r^*_{\max}$. Examining the error bands, one observes that the standard deviations for $\mathcal{S}^*$ and $\mathcal{P}^*$ consistently increase with $\delta r^*_{\max}$.

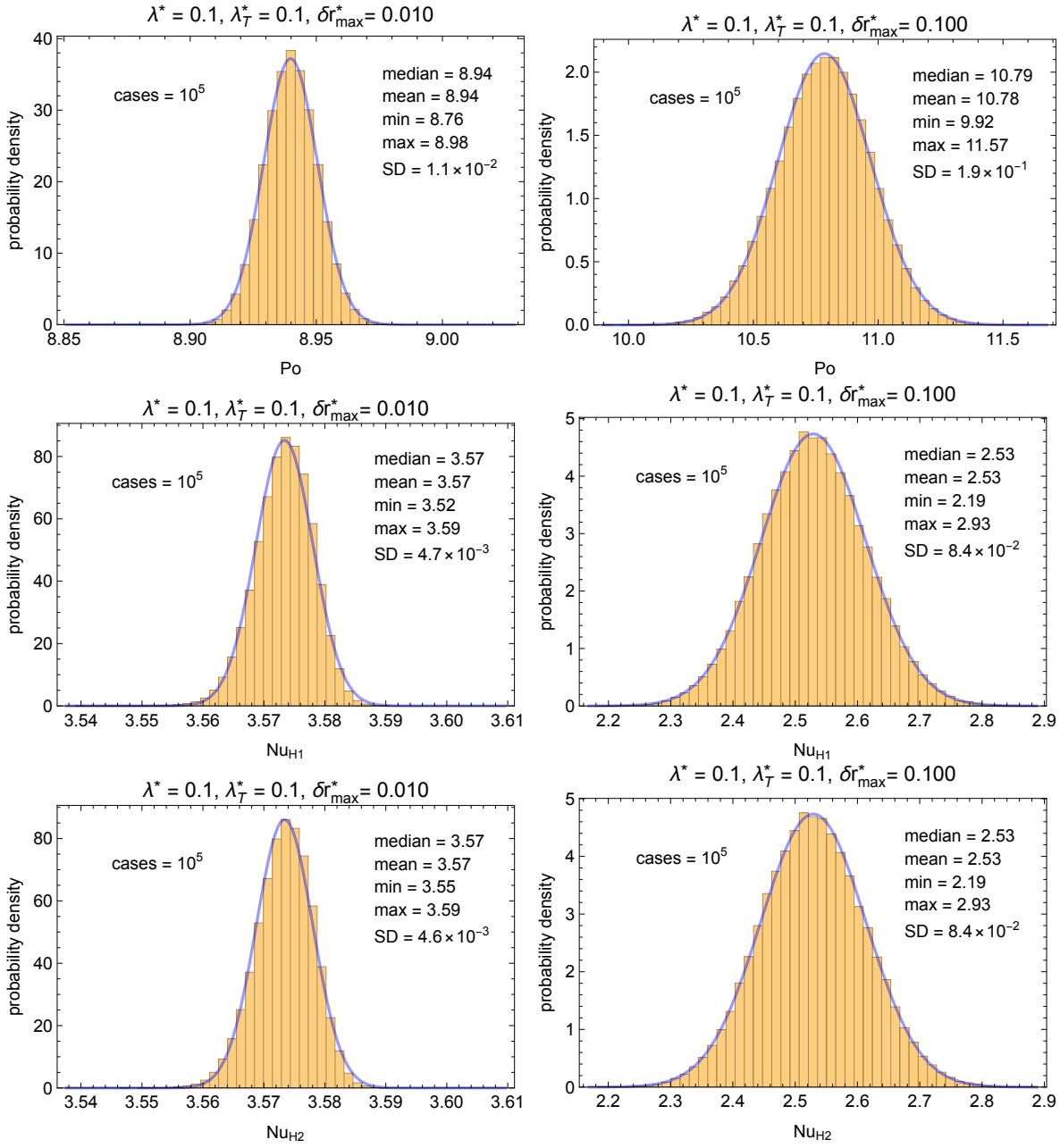

Figure 6: Histogram plots for Poiseuille and Nusselt numbers for $\lambda^* = \lambda_T^* = 0.1$ calculated for 10^5 random geometries with $n_{pts} = 100$ and $\delta r^*_{\max} = 0.1$.

Finally, when observing the effect of varying the number of boundary points, one notices that the mean $\mathcal{S}^*$ value for cases with 25 points is 1.5% smaller than the nominal value, while for cases with 50 points, this value is approximately 0.25%. This discrepancy arises from using a finite number of boundary points connected by straight lines, as the mean values of $\mathcal{S}^*$ are associated with polygons with 25 and 50 sides, rather than a true circle, resulting in slightly smaller areas. This effect is visually undetectable for geometries with 100 and 200

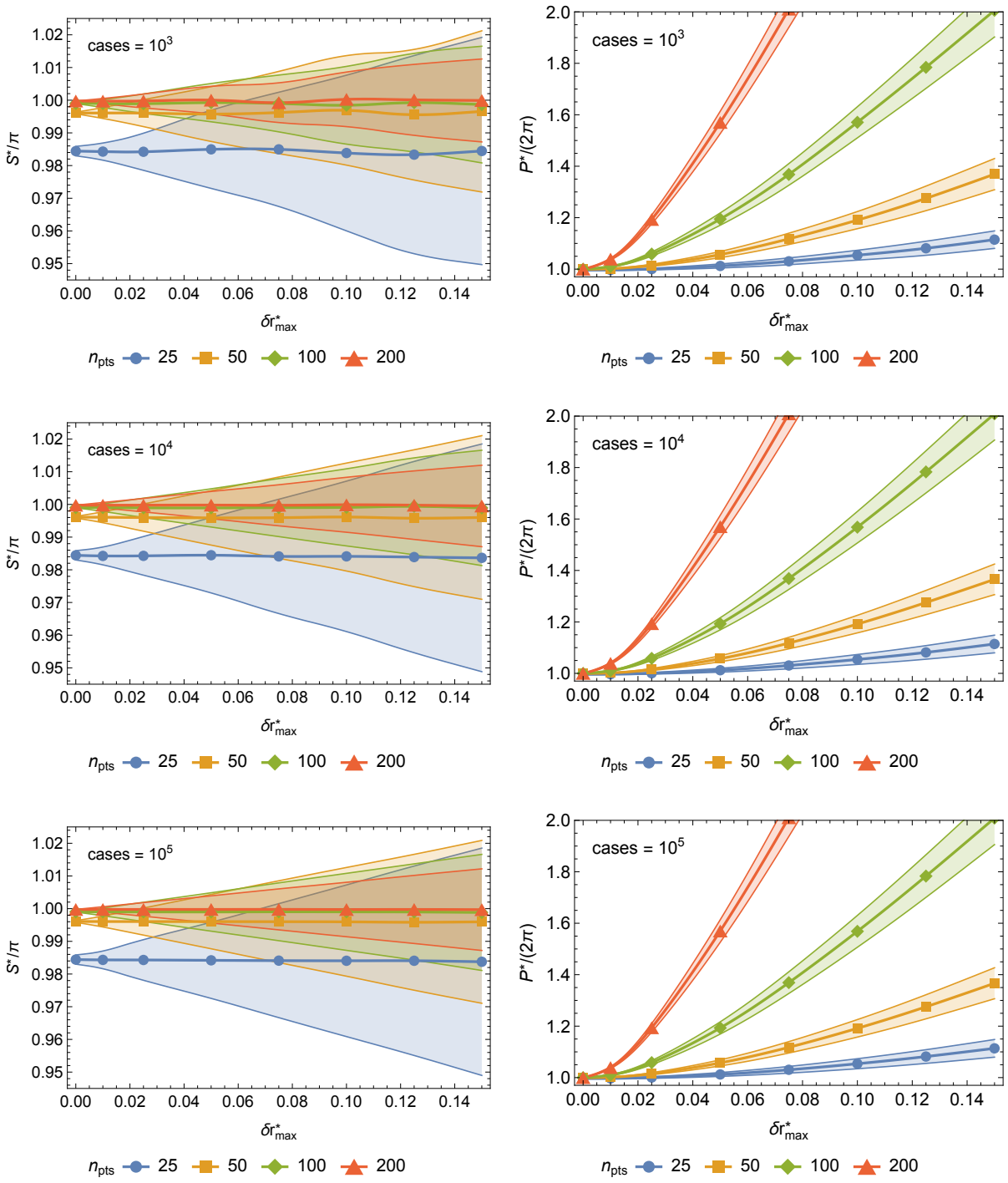

Figure 7: Error-band plots for $\mathcal{S}^*$ and $\mathcal{P}^*$ divided by their nominal values for $\lambda^* = \lambda_T^* = 0$ and points connected by straight lines.

points. Therefore, geometry cases with 100 boundary points are selected for presenting the remainder of the results in this investigation. Additionally, all subsequent analyses will use sample sizes of 10^5 geometries for each configuration, as previously mentioned.

4.3. Effect of roughness on pressure drop and heat transfer

Once an adequate number of boundary points, mesh size, and sample size are established, the following results are dedicated to analyzing the effects of increasing roughness, controlled by the parameter $\delta r^*_{\max}$, as well as the slip parameters λ^* and λ_T, on the pressure drop (i.e., Po) and heat transfer (i.e., $\mathrm{Nu_{H1}}$ and $\mathrm{Nu_{H2}}$). Figure 8 shows the variation of the Poiseuille number with the roughness parameter for different values of the slip length parameter λ^*. In addition to the actual Po values, the ratios $\mathrm{Po}/\hat{\mathrm{Po}}$ are plotted to enable comparison with the values for smooth channels. As one can observe, increasing the non-dimensional slip

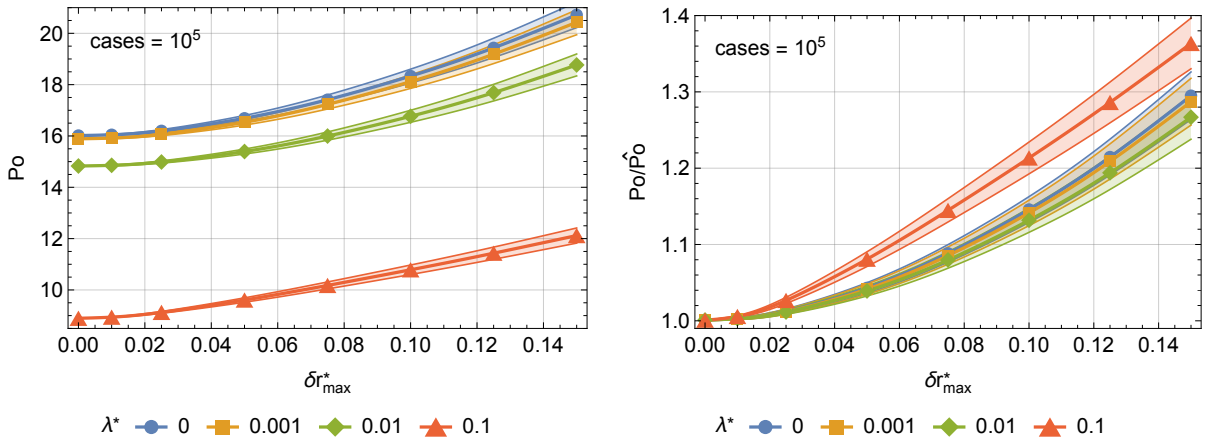

Figure 8: Variation of the Poiseuille number Po with the roughness parameter $\delta r^*_{\max}$ for different values of the velocity slip parameter λ^*.

length from 0 (no slip) to 0.1 reduces the friction factor to almost half of the value for $\lambda^* = 0$. This reduction in Po is expected and aligns with previous literature, as shear stress at the walls decreases with an increase in the velocity slip parameter. It is also notable that this reduction in Po for larger λ^* values generally occurs across all values of the roughness parameter $\delta r^*_{\max}$. When analyzing the effect of the roughness parameter on the Poiseuille number for each λ^* case, one sees that the increase in Po with $\delta r^*_{\max}$ is exponential. Median Po values are at least 25% higher than those for smooth channels when $\delta r^*_{\max} = 0.15$. This exponential trend implies that, for small roughness (e.g., around 1%), there is minimal variation in the friction factor; however, the rate of increase becomes noticeably higher as $\delta r^*_{\max}$ exceeds 2.5%. Examining the standard deviation (illustrated by the size of the error bands) reveals that it also increases with $\delta r^*_{\max}$. Accounting for this deviation, a roughness parameter of $\delta r^*_{\max} = 0.15$ can very likely result in Po exceeding nominal values by 30% for $\lambda^* = 0$ (no slip) and around 40% for $\lambda^* = 0.1$. These observations indicate that, although

increasing the slip parameter λ^* reduces the friction factor, the case with a higher λ^* value is more significantly impacted by the roughness parameter.

The following results examine the effects of the roughness parameter on heat transfer. Figure 9 displays the variations of $\mathrm{Nu_{H1}}$ and $\mathrm{Nu_{H2}}$ for different values of λ^*, with λ_T^* set to zero. As observed, increasing λ^* leads to higher Nusselt values due to elevated mass flow

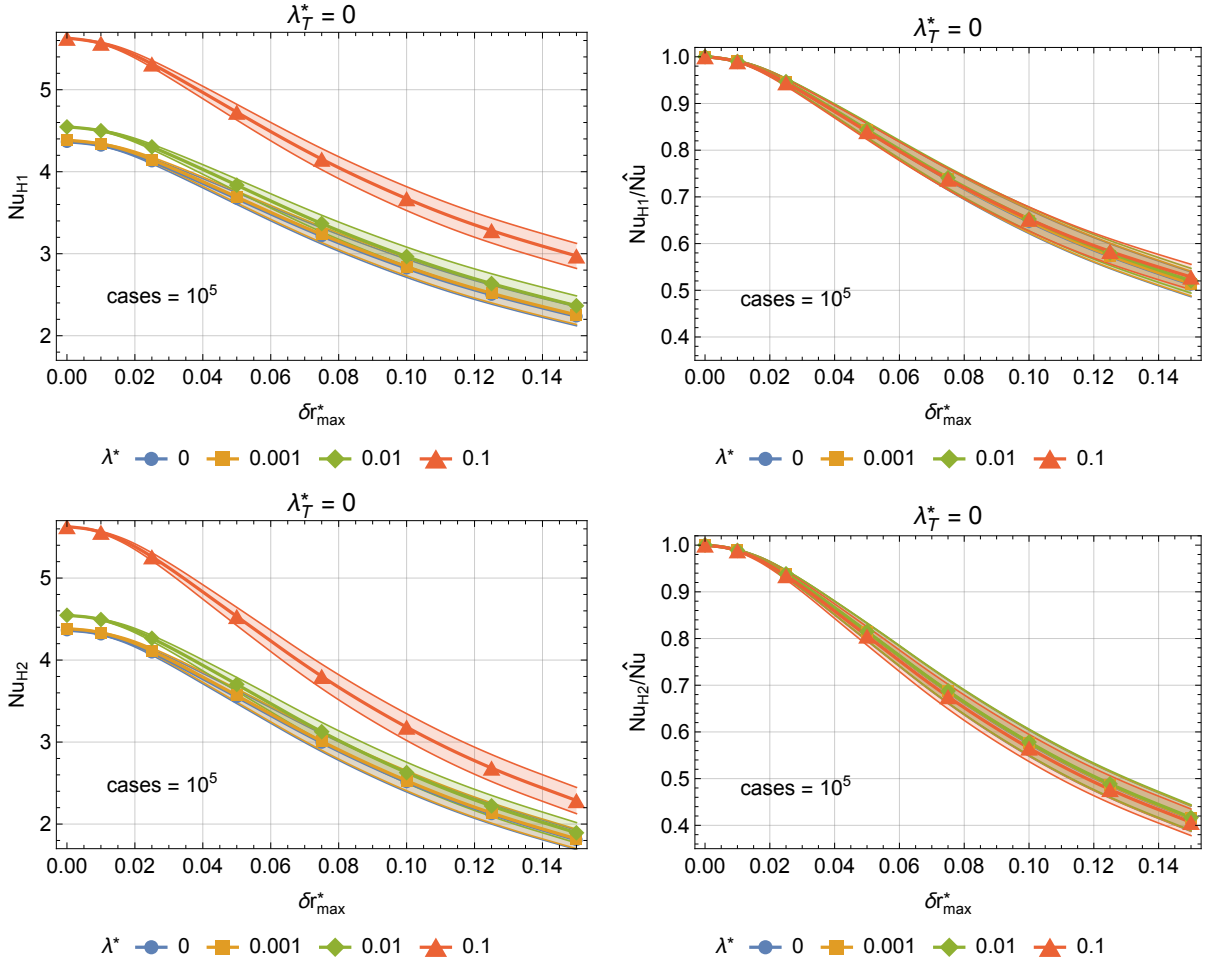

Figure 9: Variation of the Nusselt numbers $\mathrm{Nu_{H1}}$ and $\mathrm{Nu_{H2}}$ with the roughness parameter $\delta r^*_{\max}$ for $\lambda_T^* = 0$ and different values of the velocity slip parameter λ^*.

rates near the wall, resulting from the velocity slip condition. Naturally, this increase occurs as there is no additional thermal resistance caused by a temperature jump condition at the wall. Examining the effect of the roughness parameter $\delta r^*_{\max}$, one notices a significant drop in the Nusselt numbers. Compared to the variations seen for the Poiseuille number, the relative drop in the Nusselt numbers is considerably larger than the increase observed in Po, indicating that roughness has a stronger impact on the heat transfer rate than on pressure drop. Although the observed variations are greater for the Nusselt numbers, a similar trend to that seen for Po is noted here: for small values of $\delta r^*_{\max}$ (around 1%), variations in

the Nu values remain small; however, as $\delta r^*_{\max}$ increases further, a substantial drop in Nu follows. Finally, when comparing the effect of $\delta r^*_{\max}$ on $\mathrm{Nu}_{\mathsf{H1}}$ and $\mathrm{Nu}_{\mathsf{H2}}$, one notices that the latter is more significantly impacted by an increase in $\delta r^*_{\max}$. While the Nusselt values decrease by nearly 50% under the H1 condition, the reduction for $\mathrm{Nu}_{\mathsf{H2}}$ approaches 60%. The lower Nu values observed for the H2 condition can be attributed to the fact that a highly irregular boundary results in hotter spots in regions with reduced flow rates, such as outward boundary spikes, which can lead to a higher average boundary temperature.

The next results account for the effect of individually varying the temperature jump condition parameter λ^*_T, with the velocity slip parameter λ^* fixed at 0.1, as portrayed in Figure 10. As one can observe, for $\lambda^*_T \leq 0.01$, the Nusselt numbers remain higher than those

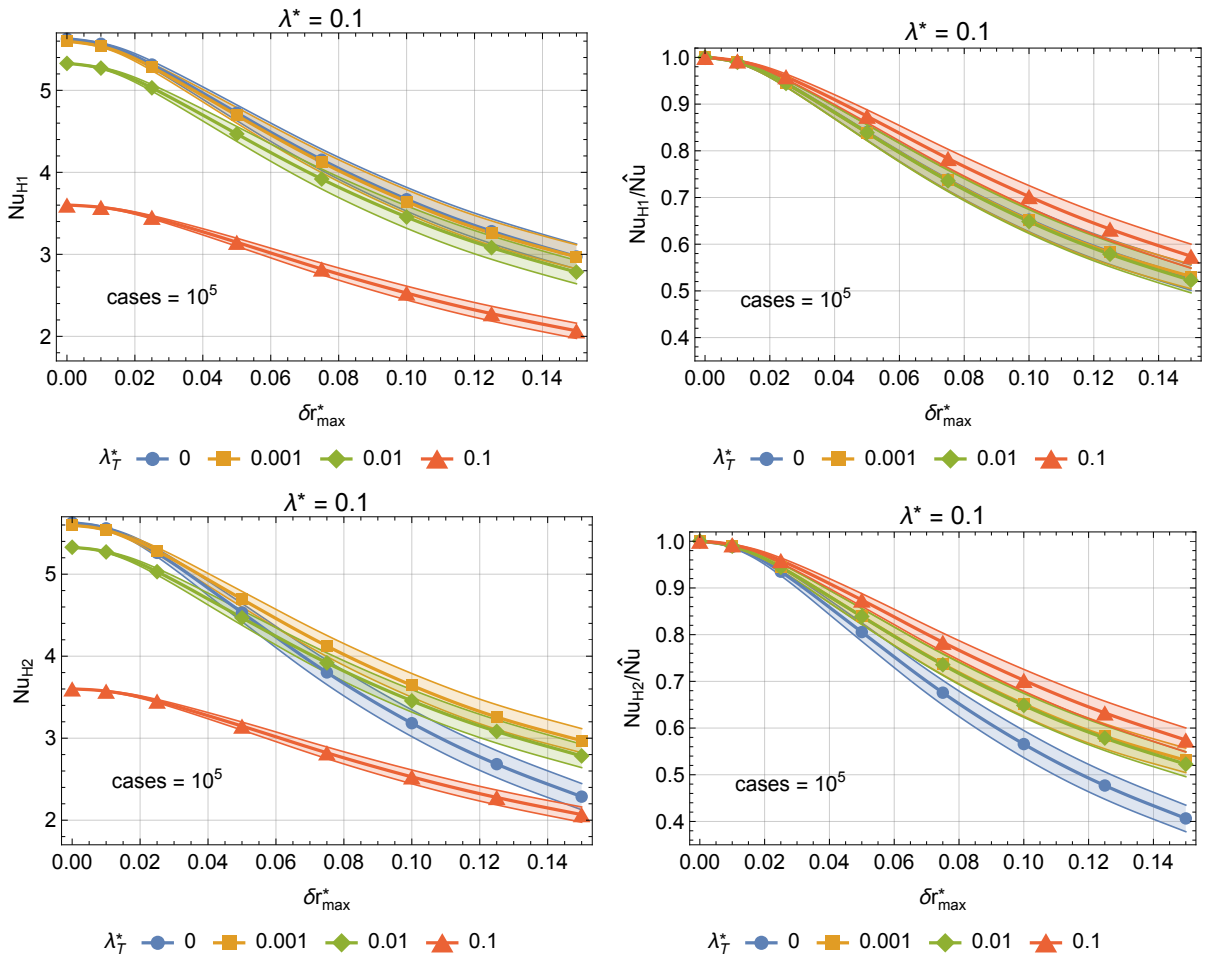

Figure 10: Variation of the Nusselt numbers $\mathrm{Nu}_{\mathsf{H1}}$ and $\mathrm{Nu}_{\mathsf{H2}}$ with the roughness parameter $\delta r^*_{\max}$ for $\lambda^*_T = 0.1$ and different values of the temperature jump parameter λ^*_T.

for cases with no slip and no temperature jump (i.e., $\lambda^* = \lambda^*_T = 0$), due to the large value of λ^* used in these simulations. However, when λ^*_T reaches 0.1, the Nusselt number values become lower than in the $\lambda^* = \lambda^*_T = 0$ case, indicating that the additional thermal resistance from the temperature jump has a stronger effect on heat transfer than the increased mass

flow rate near the wall resulting from the velocity slip condition. When examining the effect of $\delta r^*_{\max}$ on the Nusselt values, as similarly observed in Figure 9, the reduction in the Nusselt numbers due to increasing roughness is notably stronger for the H2 boundary condition. Nevertheless, the additional thermal resistance associated with the temperature jump parameter λ^*_T reduces the impact of roughness on the Nusselt values. Specifically, as λ^*_T increases, the relative reduction in $\mathrm{Nu}_{\mathsf{H1}}$ and $\mathrm{Nu}_{\mathsf{H2}}$ tends to be smaller. This effect is particularly strong for the H2 condition, where the Nusselt number reduction is much greater when $\lambda^*_T = 0$ compared to $\lambda^*_T = 0.1$. Despite these trends, the relative reduction in cases with $\lambda^*_T = 0.01$ and $\lambda^*_T = 0.001$ is almost identical and appears similar to the case with $\lambda^*_T = 0$ under the H1 condition.

Lastly, Figure 11 shows the variation of the Nusselt numbers with the roughness parameter $\delta r^*_{\max}$, considering the case where $\lambda^* = \lambda^*_T$, such that both the velocity slip and temperature jump parameters are varied simultaneously. As one can observe, under the H1

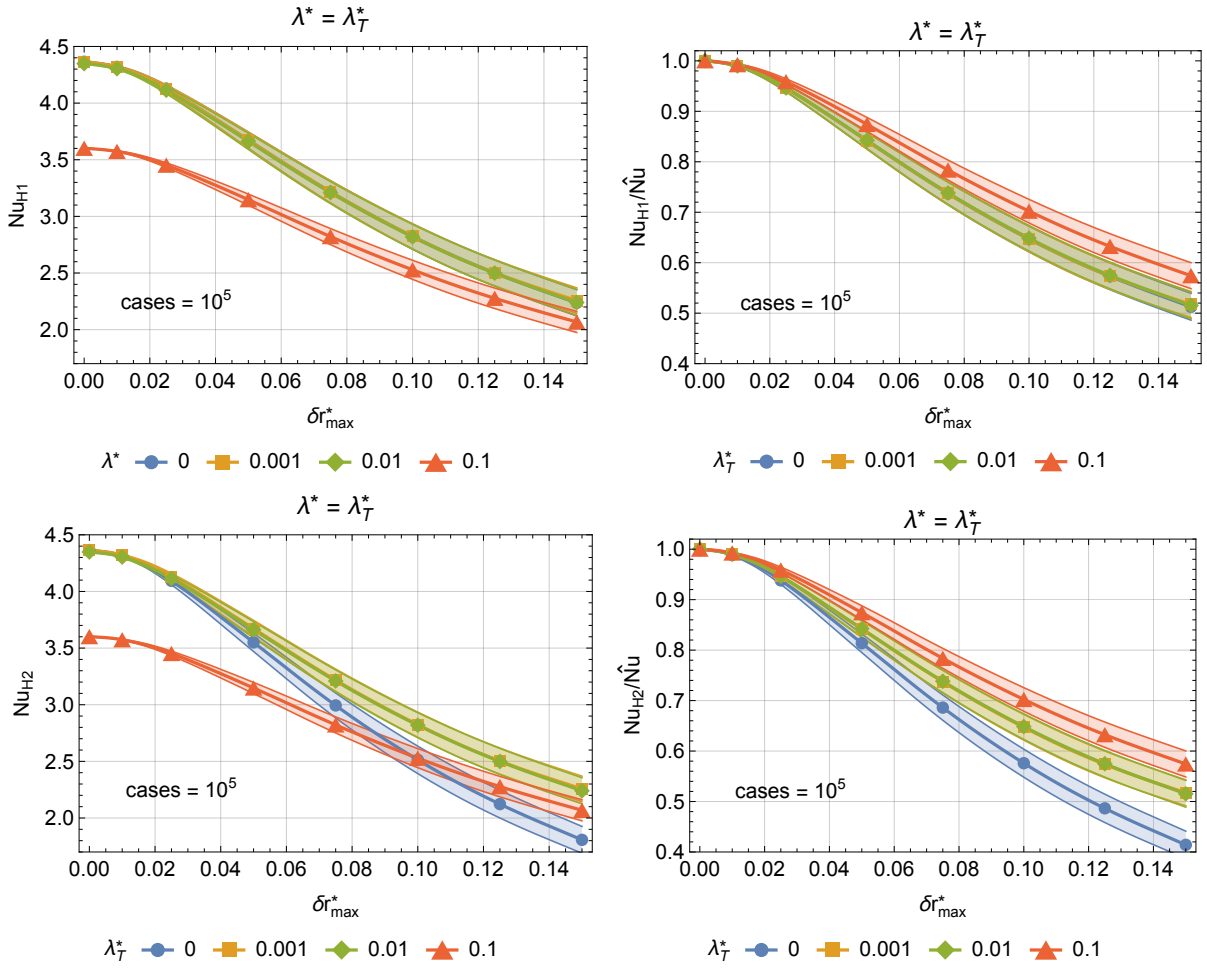

Figure 11: Variation of the Nusselt numbers $\mathrm{Nu}_{\mathsf{H1}}$ and $\mathrm{Nu}_{\mathsf{H2}}$ with the roughness parameter $\delta r^*_{\max}$ for $\lambda^*_T = \lambda^*$.

condition and for small λ^* values ($\lambda^* \leq 0.01$), the Nusselt number curves nearly overlap,

indicating that the positive contribution to the heat transfer rate from the increased near-wall mass flow rate is balanced by the negative contribution from the thermal resistance associated with the temperature jump, and this balance holds for all values of $\delta r^*_{\max}$. However, when λ^* and λ^*_T are increased to 0.1, the additional thermal resistance outweighs the effect of the higher near-wall mass flow rate. For the H2 condition, a similar trend is seen, with the main difference occurring in the case with no slip and no temperature jump (i.e., $\lambda^* = \lambda^*_T = 0$). This can again be attributed to the effect of hotspots along the irregular boundary, which tend to be more intense for $\lambda^*_T = 0$. Combined with the lower near-wall mass flow rate (compared to cases with $\lambda^* > 0$), this makes the no-slip, no temperature-jump case the one with the greatest reduction in the Nusselt number value in this figure.

5. Acknowledgements

The author L.A.S. would like to acknowledge the financial support provided by the Brazilian Government Funding Agencies, CNPq, and FAPERJ.

6. Conclusions

This study has been devoted to the investigation of the impact of geometric uncertainties due to roughness on heat transfer and fluid flow in microchannels, by examining how these effects varied with slip flow and temperature jump conditions. A numerical model was developed for laminar, fully developed flow in nominally circular microchannels with randomly varied boundary shapes, controlled by the roughness parameter, $\delta r^*_{\max}$. The analysis contemplated traditional H1 and H2 heating conditions, along with the effects of slip length (λ^*) and temperature jump (λ^*_T) parameters.

To ensure consistency given the randomly generated geometries, results were calculated across a large number of cases for each configuration, defined by specific values of $\delta r^*_{\max}$, λ^*, and λ^*_T. A sample size analysis confirmed that a substantial number of cases was necessary to avoid oscillations associated with smaller samples. Each sample was verified to follow a normal distribution, and an analysis of the variation in median values and standard deviation with $\delta r^*_{\max}$ was performed.

The results demonstrated that increasing $\delta r^*_{\max}$ leads to a higher friction factor (i.e., higher Poiseuille number) and lower Nusselt numbers, with heat transfer being more significantly impacted by roughness than pressure drop. Additionally, under the H2 heating condition, the effects were notably stronger than under the H1 condition. Although the observed trend of decreasing Nusselt numbers with increasing roughness may initially appear counterintuitive—since higher roughness levels increase surface area, potentially enhancing heat transfer rates—the reduced velocity near the wall associated with greater roughness has the opposite effect, lowering heat transfer rates. This results in a competition between these two opposing effects, with the presented analysis demonstrating that the reduction in heat transfer due to lower near-wall velocity dominates, leading to an overall decrease in heat transfer despite the increased surface area. Furthermore, the influence of the velocity slip parameter λ^* and the temperature jump parameter λ^*_T revealed that while higher λ^*

values lowered the friction factor, they were more sensitive to roughness, whereas higher λ_T^* values increased thermal resistance, with lower λ_T^* cases being more affected by roughness.

These findings indicate that, even for laminar flow, the small hydraulic diameters typical of microchannels allow roughness to substantially influence both the friction factor and Nusselt numbers. Despite such insights, this analysis represents an initial step toward understanding roughness effects in microchannels, where roughness was characterized by a single parameter. Further research into a more detailed quantification of roughness in microchannels remains essential.

References

[1] J. Nikuradse, et al., Laws of flow in rough pipes, Technical Report, National Advisory Committee for Aeronautics Washington, DC, 1950.

[2] W. Peiyi, W. Little, Measurement of friction factors for the flow of gases in very fine channels used for microminiature joule-thomson refrigerators, Cryogenics 23 (1983) 273–277.

[3] G. M. Mala, D. Li, Flow characteristics of water in microtubes, International journal of heat and fluid flow 20 (1999) 142–148.

[4] S. Kandlikar, Roughness effects at microscale–reassessing nikuradse's experiments on liquid flow in rough tubes, Bulletin of the polish academy of sciences technical sciences (2005) 343–349.

[5] S. G. Kandlikar, Exploring roughness effect on laminar internal flow–are we ready for change?, Nanoscale and Microscale Thermophysical Engineering 12 (2008) 61–82.

[6] P. Wu, W. Little, Measurement of the heat transfer characteristics of gas flow in fine channel heat exchangers used for microminiature refrigerators, Cryogenics 24 (1984) 415–420.

[7] X. Peng, G. Peterson, B. Wang, Heat transfer characteristics of water flowing through microchannels, Experimental Heat Transfer An International Journal 7 (1994) 265–283.

[8] S. Weaver, M. D. Barringer, K. A. Thole, Microchannels with manufacturing roughness levels (2011).

[9] S. Mehendale, A. Jacobi, R. Shah, Fluid flow and heat transfer at micro-and meso-scales with application to heat exchanger design (2000).

[10] M. Gad-el Hak, The fluid mechanics of microdevices—the freeman scholar lecture (1999).

[11] J.-J. Shu, J. Bin Melvin Teo, W. Kong Chan, Fluid velocity slip and temperature jump at a solid surface, Applied Mechanics Reviews 69 (2017) 020801.

[12] H. Sun, M. Faghri, Effect of surface roughness on nitrogen flow in a microchannel using the direct simulation monte carlo method, Numerical Heat Transfer: Part A: Applications 43 (2003) 1–8.

[13] C. Kleinstreuer, J. Koo, Computational analysis of wall roughness effects for liquid flow in microconduits, J. Fluids Eng. 126 (2004) 1–9.

[14] Z. Duan, Y. Muzychka, Effects of corrugated roughness on developed laminar flow in microtubes (2008).

[15] R. K. Shah, A. L. London, Longitudinal fins and twisted tapes within ducts (chapter XVI), in: R. Shah, A. London (Eds.), Laminar Flow Forced Convection in Ducts, Academic Press, 1978, pp. 366–384.

[16] A. Sadeghi, H. Salarieh, M. H. Saidi, A. A. Mozafari, Effects of corrugated roughness on gaseous slip flow forced convection in microtubes, Journal of Thermophysics and Heat Transfer 25 (2011) 262–271.

[17] H. Bruus, Theoretical Microfluidics, Oxford University Press, 2007.

[18] R. K. Shah, A. L. London, Laminar Flow Forced Convection in Ducts, in: Advances in Heat Transfer, Academic Press, 1978.

[19] A. Barletta, Fully developed laminar forced convection in circular ducts for power-law fluids with viscous dissipation, International Journal of Heat and Mass Transfer 40 (1996) 15–26.